

Article

Iron-Decorated Nitrogen/Boron co-Doped Reduced Graphene Oxide Aerogel for Neutral Rechargeable Zn-Air Batteries

Yuyun Irmawati ^{1,2,3}, Falihah Balqis ⁴, Pilar Bela Persada ⁴, Fredina Destyorini ³, Rike Yudianti ³, Ferry Iskandar ^{2,5,6}  and Afriyanti Sumboja ^{4,6,*} 

- ¹ Doctoral Program of Nanosciences and Nanotechnology, Graduate School, Institut Teknologi Bandung, Jl. Ganesha 10, Bandung 40132, Indonesia
- ² Research Center for Nanosciences and Nanotechnology (RCNN), Institut Teknologi Bandung, Jl. Ganesha 10, Bandung 40132, Indonesia
- ³ Research Center for Advanced Materials, National Research and Innovation Agency (BRIN), Kawasan Puspiptek Gedung 440, Tangerang Selatan 15314, Indonesia
- ⁴ Material Science and Engineering Research Group, Faculty of Mechanical and Aerospace Engineering, Institut Teknologi Bandung, Jl. Ganesha 10, Bandung 40132, Indonesia
- ⁵ Department of Physics, Faculty of Mathematics and Natural Sciences, Institut Teknologi Bandung, Jl. Ganesha 10, Bandung 40132, Indonesia
- ⁶ Collaboration Research Center for Advanced Energy Materials, National Research and Innovation Agency—Institut Teknologi Bandung, Jl. Ganesha 10, Bandung 40132, Indonesia
- * Correspondence: sumboja@itb.ac.id

Abstract: Zn-air batteries (ZABs) with neutral electrolytes offer a significantly longer lifespan and better recyclability than alkaline ones. However, low-performance bifunctional catalytic activities for oxygen reduction or evolution reaction (i.e., ORR/OER) in neutral electrolytes still hamper their development. Here, we report iron nanoparticle-decorated nitrogen/boron co-doped reduced graphene oxide aerogel (Fe-NBrGO) with distinguished ORR/OER activity, enabling its application in neutral rechargeable ZABs. Taking advantage of the formation of 3D porous structure of graphene aerogel, N/B-moieties active sites, and Fe-containing active sites, Fe-NBrGO exhibits high ORR onset potential (1.074 and 0.817 V) and adequate OER overpotential (476 and 615 mV) in alkaline and neutral electrolytes, respectively. Fe-NBrGO enables the production of a neutral-ZAB with 34 mW cm⁻² in peak power density and remains stable for a 284 h (~852 cycles) cycling test. This research highlights the rational design of highly active oxygen catalysts for the widespread implementation of new energy storage technologies.

Keywords: electrocatalysts; heteroatom-doped carbon; OER; ORR; ZABs



Citation: Irmawati, Y.; Balqis, F.; Persada, P.B.; Destyorini, F.; Yudianti, R.; Iskandar, F.; Sumboja, A. Iron-Decorated Nitrogen/Boron co-Doped Reduced Graphene Oxide Aerogel for Neutral Rechargeable Zn-Air Batteries. *Batteries* **2023**, *9*, 356. <https://doi.org/10.3390/batteries9070356>

Academic Editors: Meng-Fang Lin, Alice Lee-Sie Eh, Wenbin Kang and Lulu Xu

Received: 24 March 2023

Revised: 24 June 2023

Accepted: 1 July 2023

Published: 4 July 2023



Copyright: © 2023 by the authors. Licensee MDPI, Basel, Switzerland. This article is an open access article distributed under the terms and conditions of the Creative Commons Attribution (CC BY) license (<https://creativecommons.org/licenses/by/4.0/>).

1. Introduction

Depletion of fossil fuel resources and an increase in concerns over environmental problems have spurred the utilization of sustainable and environmentally friendly energy systems [1,2]. Among these technologies, Zn-air batteries (ZABs) have been projected to be a future candidate for energy storage systems because of their inherent safety and high energy density [3]. However, the common use of alkaline electrolytes still limits the cycle life of rechargeable ZABs since high alkalinity electrolytes can degrade carbon-based air cathodes [4,5], accelerate the formation of Zn dendrites [6], and produce carbonate ions that decrease the conductivity of the electrolyte [7,8], hence shortening the battery life. In addition, the corrosiveness of alkaline electrolytes impedes the practical application of ZABs in wearable electronics [9].

Currently, ZABs with neutral electrolytes are viewed as feasible alternatives for addressing the abovementioned concerns of alkaline media [6,9,10]. Nevertheless, there might be a significant drop in catalytic activity in neutral electrolytes that is reportedly associated with low ionic conductivity and low concentration of H⁺/OH⁻ ions

in neutral conditions [6,10]. Therefore, oxygen catalysts with desirable oxygen reduction/evolution reaction (ORR/OER) activities in neutral electrolytes are highly advised to support their development.

In stark contrast to the high cost and limited resources of Pt and Ir-based catalysts, non-metal heteroatom-doped carbon materials have low fabrication costs and abundant resources, making them promising as oxygen catalysts. Moreover, they possess high electrical conductivity and a tunable electronic structure [11]. Nitrogen (N) and boron (B) are predicted as ideal dopants among the heteroatom dopants since they possess different electronegativity values ($\chi_N = 3.04$, $\chi_B = 2.04$, and $\chi_C = 2.25$) but relatively similar atomic radii to carbon atoms [12]. Introducing high electronegativity of nitrogen atoms results in positively charged adjacent carbon atoms, which serve as the adsorption sites to O_2 molecules [12]. Meanwhile, doping boron atoms with low electronegativity produces active sites from the positively charged boron species [12,13].

Unlike solely N-doped or B-doped carbon, previous studies reported improved catalytic activity in alkaline electrolytes by dual dopants of N and B atoms [13–15]. An N/B co-doped carbon nanosheet was obtained via pyrolysis of a mixture consisting of glucose, guanidine carbonate, boric acid, and sodium chloride [13]. It showed higher half-wave potentials ($E_{1/2} = 0.8$ V) than its single N-doped (0.78 V) or B-doped (0.7 V) counterparts. The electron-deficient feature of B atoms produced more favorable sites for O_2 adsorption, accelerating reaction kinetics in ORR [13]. Similarly, Chen et al. reported an increase in ORR activity of dual N/B co-doped carbon [15]. They obtained onset potential (E_{onset}) of about 0.986 V for N/B co-doped carbon, compared to ~0.946 and ~0.896 V for those with solely N- or B-doped carbon, respectively. The presence of N and B dopants destroys the charge neutrality of the carbon structure, in which pyridinic-N and BC_3 active sites play an important role in elevating the catalytic activities [15,16]. In addition, dual N/B co-doped carbon may also result in a B-N configuration that serves as additional ORR active sites [17]. The higher electronegativity of N can polarize the nearby B atom, promoting the adsorption of oxygen intermediates. Cheng et al. positively shifted E_{onset} to 0.960 V for N/B co-doped carbon in alkaline electrolyte, compared to 0.832 and 0.818 V for N-doped and B-doped carbon, respectively [17].

Despite showing adequate catalytic activity in alkaline electrolytes, only limited studies have explored the application of N/B co-doped carbon in neutral conditions [17,18]. In neutral electrolytes, there is still a necessity to overcome the low kinetic activity of N/B co-doped carbon [18]. Metal-free and metal-containing active sites should coexist in developing Pt-free ORR catalysts with satisfactory performance across a wide pH range [1,19]. This is due to the fact that most metal-free active sites (e.g., pyridinic-N) undergo protonation under non-alkaline conditions that reduce their catalytic performance [20]. Particularly in neutral electrolytes, ORR activity was claimed to be partly driven by both metal-free and metal-containing active sites [21]. Hence, introducing metal-containing actives sites ensures sufficient ORR activity in neutral pH [22]. The presence of metal species alters the work function of the carbon matrix, hence decreasing oxygen adsorption energy and increasing catalytic activity [23]. In addition, optimizing the catalytic activities also requires a fast and uniform distribution of reactant into the active sites. Aerogel with a 3D porous structure is suitable for this requirement owing to its micro-meso-macropores configuration [24–26].

Herein we fabricated N/B co-doped reduced graphene oxide aerogel decorated with iron nanoparticles (Fe-NBrGO) as oxygen catalysts in alkaline and neutral electrolytes. Employing a simple hydrothermal synthesis and pyrolysis process, the obtained sample shows a porous 3D carbon aerogel with homogeneously distributed iron nanoparticles. The overlapping of graphene sheets results in numerous accessible active sites, highlighting graphene aerogel's interconnected 3D porous architectures. In addition, the uniform distribution of iron nanoparticles improves the catalytic activity in alkaline and neutral electrolytes. Highlighting the merits of neutral electrolytes to lengthen the batteries' cyclability, a neutral rechargeable ZAB with Fe-NBrGO can deliver a stable charge-discharge cycling test of up to ~852 cycles (284 h). It significantly outperforms the stability of alkaline

ZAB (174 cycles/58 h). This research sheds new insight into the fabrication of highly active oxygen catalysts for the widespread implementation of new energy conversion and storage technologies.

2. Materials and Methods

Commercial graphite powder was used to synthesize colloidal graphene oxide (GO) with a concentration of ~4 mg/mL [27]. Iron nanoparticle-decorated N/B co-doped graphene aerogel (Fe-NBrGO) was prepared by dissolving 1.25 g urea (Smartlab), 0.25 g boric acid (Merck), and 36 mg iron nitrate (Merck) in 10 mL deionized water (DI water). The obtained solution was then mixed with 15 mL aqueous suspension of GO and ~0.5 mL ammonia solution (Merck). Subsequently, at a set temperature of 180 °C, the mixture was hydrothermally treated using a 50 mL Teflon-lined autoclave for 12 h. The synthesized sample was washed with DI water and freeze-dried to keep its porous structure. Finally, the dried sample was pyrolyzed at 900 °C (2 h) under N₂ atmosphere. As a comparison, a sample without adding iron nitrate and ammonia solution, denoted as NBrGO, was prepared with a similar process. Additional experimental data, including material characterizations, electrochemical measurements, and zinc-air battery tests, are presented in the Supplementary Materials.

3. Results and Discussion

Figure 1a depicts a schematic of the Fe-NBrGO synthesis procedure via hydrothermal synthesis and pyrolysis processes. GO, urea, boric acid, and iron nitrate were used as carbon, nitrogen, boron, and iron precursors, respectively. Numerous oxygen functional groups on the surface of GO produced a stable starting suspension, as shown in the digital photograph. As the hydrothermal synthesis proceeds (180 °C, 12 h), oxygen functional groups are reduced, resulting in a reduced graphene oxide (rGO) [24]. This reduction is proven by the disappearance of the GO signature peak at 10° (Figure 1b), which was replaced by a broad peak at ~26°, indexed to the (002) plane of carbon (PDF 075-1621) [26,28]. Reduction of GO increases the π–π interactions between the nanosheets, leading to the self-assembly of 3D rGO-based aerogel [29]. During hydrothermal synthesis, iron nanoparticles may form and integrate into the 3D rGO structure, as shown by several peaks at ~24°, 33°, 36°, 49°, and 54°, which correspond to Fe₂O₃ (PDF 089-0596) in the diffractograms of Fe-NBrGO before pyrolysis (Figure 1b).

After pyrolysis, Fe-NBrGO shows three different iron phases: Fe metal (PDF#006-0696), Fe₃C (PDF#035-0772), and Fe₃O₄ (PDF#019-0629), indicating a reduction of the Fe₂O₃ phase (Figure 1b) [30,31]. These iron phases may serve as active sites during the ORR/OER process [31–33]. For comparison, a similar sample but without adding iron nitrate (i.e., NBrGO) shows only typical peaks at ~26° and 44° as corresponding to (002) and (100) plane of carbon (PDF#075-1621) (Figure S1). Notably, there is a positive shift in the (002) peak of pyrolyzed Fe-NBrGO to a higher 2 theta (26.14°) compared to Fe-NBrGO before pyrolysis and pyrolyzed NBrGO (~25.7°) (Figure S2). After pyrolysis, a positive shift in the 2 theta indicates a reduction in carbon d-spacing of Fe-NBrGO from 0.347 to 0.341 nm. During pyrolysis, Fe nanoparticles may facilitate the rearrangement of carbon structure, shifting the (002) peak closer to the peak of graphite (~26.5°) [34]. Reducing the d-spacing of carbon structure may increase the electrical conductivity, thus fastening the electron transfer during the catalytic reaction [35].

The degree of carbon defects of pyrolyzed samples, compared to the pristine GO, was then evaluated using Raman spectroscopy. From Figure 1c, GO, NBrGO, and Fe-NBrGO have two typical peaks of the carbon structure. A peak at ~1345 cm⁻¹ represents the sp³ defects structure (D peak), while a peak at ~1590 cm⁻¹ illustrates the graphitic carbon sp² structure (G peak) [36]. By fitting the Raman spectra (Figure S3), the integrated area below the D to G peaks was calculated to predict the degree of carbon defects (I_D/I_G) [37]. NBrGO and Fe-NBrGO have a higher I_D/I_G (i.e., 1.80 and 1.88) than pristine GO (1.47). This indicates that introducing N and B dopants can generate more defects within the carbon

matrix, which also agrees with the previous studies [15,38]. A higher defective carbon structure has been reported to be beneficial for catalytic performance since the structure can significantly increase the adsorption sites of oxygen intermediates [39,40].

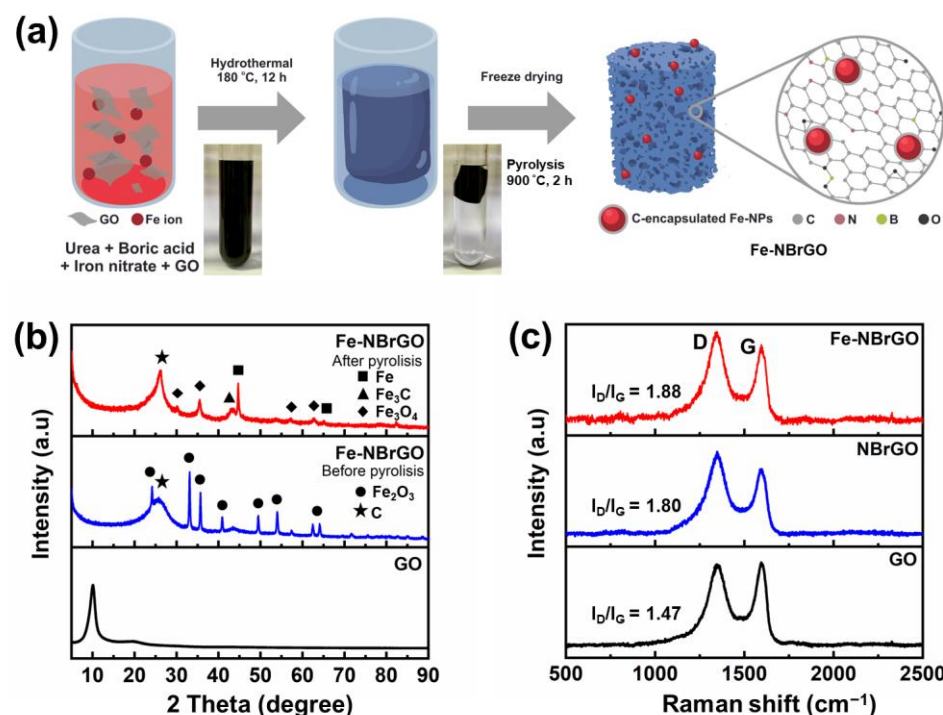


Figure 1. (a) Schematic illustration of Fe-NBrGO synthesis. (b) XRD patterns of GO and Fe-NBrGO before/after pyrolysis. (c) Raman spectra of GO and pyrolyzed NBrGO and Fe-NBrGO samples.

The 3D porous structure of the rGO-based aerogel samples was then evaluated using scanning electron microscopy (SEM) and N₂ desorption and adsorption measurement. Figure 2a shows that NBrGO possesses a porous structure produced by reassembling rGO nanosheets during the hydrothermal process. Applying the Brunauer–Emmett–Teller (BET) calculation method, NBrGO has a BET surface area of 553 m² g⁻¹ with bimodal micro/mesoporosity that peaks at 2–4 nm (Figure 2c). Unlike NBrGO, spherical Fe nanoparticles are easily distinguished in the aerogel of Fe-NBrGO (Figures 2b and S4b). In addition, from the energy dispersive X-ray analysis (EDX-mapping), Fe nanoparticles are homogeneously distributed on the aerogel substrate (Figure S4c). The presence of Fe nanoparticles allows the expansion in the pore size, producing hierarchical mesopores with ~3, 9, and 20 nm pore sizes (Figure 2c). The high content of mesopores is advantageous as it can accelerate the mass transfer during the reaction [25,41]. However, Fe-NBrGO experienced a decrease in the surface area to 300 m² g⁻¹. This may be due to the loss of the external surface, as Fe nanoparticles are predominantly distributed on the surface [42,43].

The internal morphology of Fe-NBrGO was then analyzed using transmission electron microscopy (TEM). In agreement with the SEM images, Fe nanoparticles (29–70 nm) are uniformly distributed on the gossamer and wrinkle-like structure of rGO (Figure 2d,e), increasing the exposed active area [22]. In Figure 2f, high-resolution TEM (HRTEM) images of Fe-NBrGO show Fe nanoparticles wrapped with N-doped carbon layers with lattice fringes of 0.34 nm, corresponding to the d-spacing of (002) carbon. It has been reported that coupling between the p_z orbital of a carbon layer and the d orbital of the metal core enables a fast electron transfer from the metal core to the outer N-doped carbon layer, thereby facilitating the ORR [44,45]. In addition, the protective carbon layers also prevent direct contact between the electrolyte and metal nanoparticles, enhancing the stability of Fe-NBrGO [46,47].

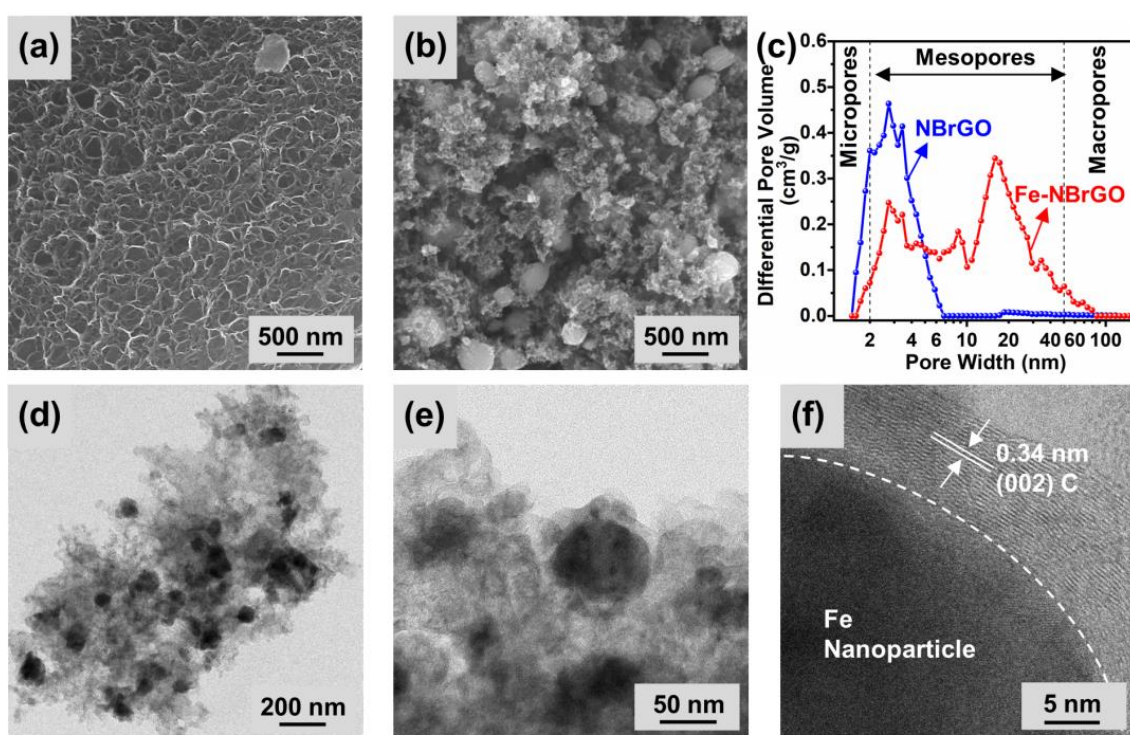


Figure 2. SEM images of (a) NBrGO and (b) Fe-NBrGO, revealing the 3D porous structure of rGO-based aerogel. (c) Pore distributions of NBrGO and Fe-NBrGO. (d,e) TEM images of Fe-NBrGO at different magnifications illustrate a uniform distribution of Fe nanoparticles. (f) HRTEM images of Fe-NBrGO revealing Fe nanoparticles coated with carbon layers.

The surface elemental compositions of Fe-NBrGO were analyzed using X-ray photoelectron spectroscopy (XPS). From the full XPS spectra, there exist C, N, B, O, and Fe in Fe-NBrGO (Figure S5). Distinct peaks at around 399 and 191 eV indicate that N and B atoms are successfully doped in the sample [15]. Then, the bonding states of N, B, and Fe are shown by deconvoluting their high-resolution spectra. In Figure 3a, the N 1s spectrum is deconvoluted into three different N-moieties: pyridinic-N (398.9 eV), graphitic-N (402 eV), and pyrrolic-N (400.8 eV) [48,49]. Among these N-moieties, the high content of graphitic-N (11%) and pyridinic-N (73%) (Supplementary Material Table S1) is preferable since both structures show high ORR activity, corresponding to an increase in limiting current density and onset potential, respectively [50,51]. Graphitic-N may boost electrical conductivity and O₂ adsorption, raising the limiting current density [51,52]. Meanwhile, pyridinic-N lowers O₂ adsorption energy, elevating the onset potential [50,53]. For the high resolution of the B 1s spectra (Figure 3b), distinguishable peaks at ~193.2, 190, and 191.3 eV are indexed to B-O, B-C, and B-N structures [54,55]. B-C and B-N have been proposed as the main active sites among B-moieties in N/B co-doped carbon [15,56].

Moreover, the XPS spectra of Fe 2p (Figure 3c) show two peaks corresponding to Fe 2p_{1/2} and Fe 2p_{3/2}. Each peak was deconvoluted into three sub-peaks consisting of Fe²⁺, Fe³⁺, and satellite. Peaks at 726.4 eV and 723.9 index to Fe³⁺ 2p_{1/2} and Fe²⁺ 2p_{1/2}, respectively, while 713.0 eV and 710.7 index to Fe³⁺ 2p_{3/2} and Fe²⁺ 2p_{3/2} [57]. Table S2 shows that the proportion of Fe²⁺ 2p_{3/2} (31%) is higher than that of Fe³⁺ 2p_{3/2} (24%). Since Fe²⁺ has a higher ORR activity than Fe³⁺ [51,58], this proportion suggests that Fe-NBrGO may have high ORR activity.

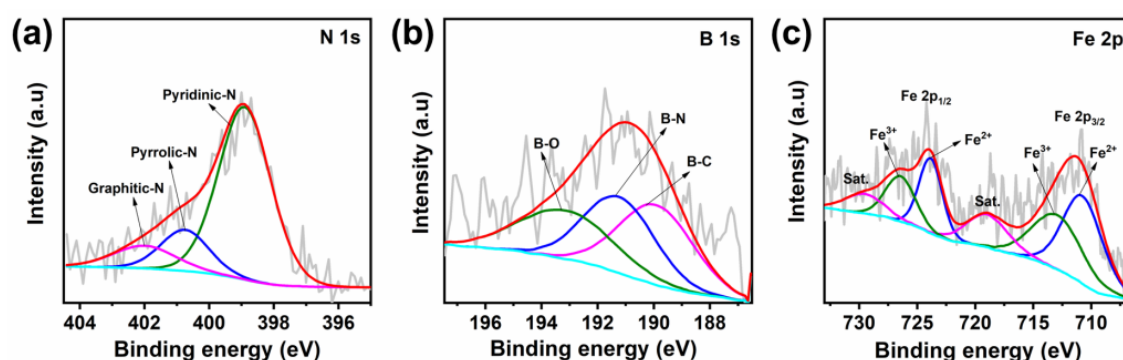


Figure 3. XPS spectra of Fe-NBrGO: deconvolution of the high resolution (a) N 1s, (b) B 1s, and (c) Fe 2p spectra.

ORR activities of Fe-NBrGO were tested using a rotating disc electrode (RDE) system in O₂-saturated electrolytes. Quantities of 0.1 M KOH and 0.1 M phosphate-buffered saline (PBS) are used to represent alkaline and neutral conditions, respectively. As a comparison, the performances of NBrGO and Pt/C were also measured. We used ORR potential at 0.1 mA cm⁻², namely onset potential (E_{onset}), limiting current density (J_{L}), and half-potential ($E_{1/2}$), as the parameters to assess ORR activity. E_{onset} and $E_{1/2}$ are given in relation to the reversible hydrogen electrode (RHE).

From Figure 4a,d, and as summarized in Table 1, Fe-NBrGO has a more positive E_{onset} and $E_{1/2}$ than NBrGO in alkaline and neutral electrolytes. Notably, in 0.1 M KOH, the E_{onset} of Fe-NBrGO (1.074 V) also surpasses the E_{onset} of Pt/C (1.054 V) and some reported metal-N/B co-doped catalysts in the literature were about 0.89–0.98 V [35,38,55,59,60], as mentioned in Table S3. The results suggest that adding Fe to the 3D porous N/B co-doped carbon significantly enhances the ORR performance. We then calculated the electrochemical double-layer capacitance (C_{dl}) of the samples at non-Faradaic regions in N₂-saturated KOH electrolyte (Figure S6) [61,62]. Notably, the trend of C_{dl} is different from the trend of the BET surface area. In spite of its lower BET surface area, Fe-NBrGO produces two times higher C_{dl} (~700 μF) than NBrGO (~400 μF). It has been reported that the value of C_{dl} was affected by not only the BET surface area but also the pore distribution and electrical conductivity of samples [63,64]. A high mesopore content advances the capacity of charge transport [58]. Meanwhile, high electrical conductivity, which may be boosted by high graphitic-N content, speeds up the transport of electron and ion percolation into the carbon matrix, hence raising the C_{dl} value. Higher C_{dl} of Fe-NBrGO indicates a higher content of accessible reaction sites of Fe-NBrGO. In other words, Fe-NBrGO has more active sites than NBrGO, which could be the reason for its higher catalytic activity. This is also in accordance with XPS measurement, in which Fe-NBrGO possesses several types of ORR active sites, such as iron-containing, N-moieties, and B-moieties active sites [56,65].

Moreover, high ORR activity by introducing Fe into N/B co-doped carbon has been previously described using DFT simulations [66,67]. A decrease in O₂ adsorption energy to −1.75 eV was found for Fe-N/B co-doped C, compared to −1.23 eV of Fe-N/C and −0.48 eV of NB/C, indicating stronger O₂ adsorption on the Fe-N/B co-doped C [66]. Adsorbed O₂ in the Fe-N/B co-doped C catalyst also experienced bond elongation by 15%, compared to ~5%, 1%, and 1.4% for Fe-N/C, NB/C, and N/C, implying the easiest O–O bond breaking during the reaction [67].

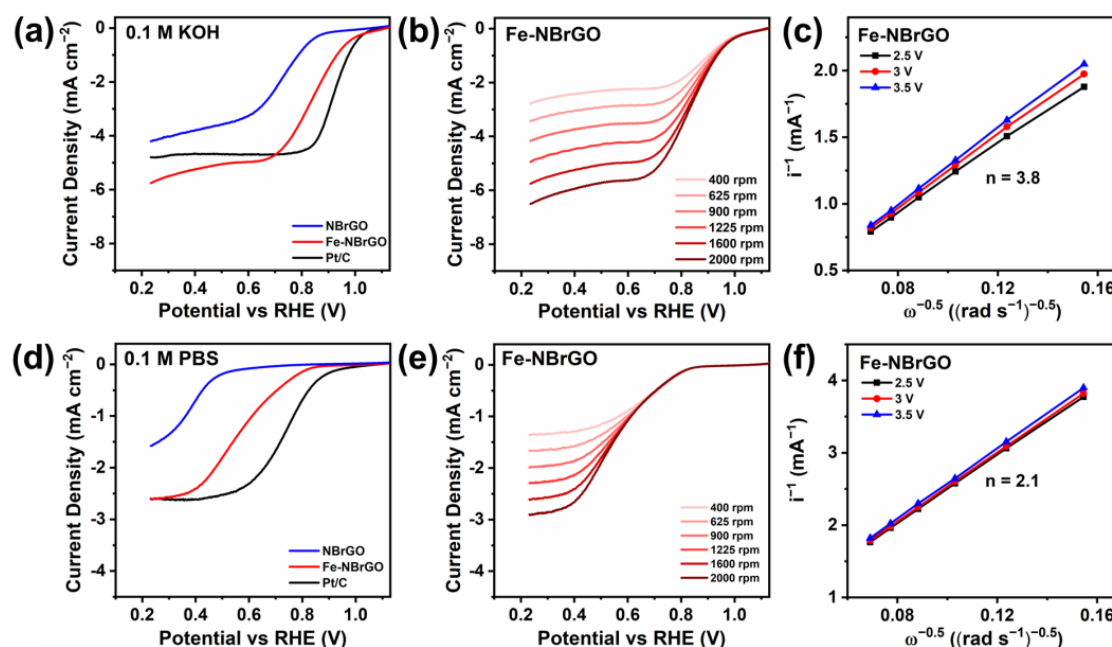


Figure 4. (a) ORR polarization curve measured at 1600 rpm of NBrGO, Fe-NBrGO, and Pt/C in alkaline electrolyte. (b) LSV profiles of Fe-NBrGO in various rotating speeds and (c) its corresponding electron transfer number in 0.1 M KOH. (d) ORR polarization curve measured at 1600 rpm of NBrGO, Fe-NBrGO, and Pt/C in neutral electrolyte. (e) LSV profiles of Fe-NBrGO in various rotating speeds and (f) its corresponding electron transfer number in 0.1 M PBS.

Table 1. ORR performance of NBrGO and Fe-NBrGO in KOH and PBS electrolytes.

Sample	E _{onset} (V vs. RHE)	E _{1/2} (V vs. RHE)	J _L (mA cm ⁻²)
0.1 M KOH			
NBrGO	0.954	0.711	4.20
Fe-NBrGO	1.074	0.826	5.75
0.1 M PBS			
NBrGO	0.566	0.382	1.58
Fe-NBrGO	0.817	0.567	2.61

The favorable ORR performance of Fe-NBrGO is also confirmed by the value of J_L , indicating the mass transport of oxygen molecules to the reaction sites [68]. Fe-NBrGO delivers the highest J_L (5.75 and 2.61 mA cm⁻²) compared to NBrGO (4.20 and 1.58 mA cm⁻²) and Pt/C (4.79 and 2.59 mA cm⁻²) in 0.1 M KOH and PBS, respectively. High J_L of Fe-NBrGO may correspond to higher content of ORR active sites and electrical conductivity by introducing iron nanoparticles into dual N/B co-doped systems. This result reconfirms the benefits of highly defective N/B co-doped carbon and the positive shift of the (002) carbon peak of Fe-NBrGO from Raman and XRD analysis. In addition, high J_L also represents the effectiveness of reactant and product transport at the catalyst/electrolyte interface to sustain continuous catalytic reactions [69].

The kinetic process of Fe-NBrGO was also evaluated using a set of LSV curves at different rotation speeds, as shown in Figure 4b,e. Higher rotation speed causes a progressive rise in the J_L , attributed to enhancing the electrode surface diffusion rate [35]. This data set is used to construct a Koutecky–Levich (K-L) plot to estimate the average electron transfer number (n). Fe-NBrGO shows a linear K-L plot at different potentials with an average n of 3.8 (Figure 4c), indicating the domination of a highly efficient four-electron pathway in alkaline media. Nevertheless, Fe-NBrGO shows an average n of 2.1, representing the prominence of reduction reaction via a two-electron pathway in neutral pH (Figure 4f).

Notably, all catalysts experience a decrease in the ORR activity in neutral media. The ORR mechanism in electrolytes with pH below 11 tends to follow the mechanism in acidic conditions [20]; thus, ORR activity decreases as H^+ concentration drops significantly in neutral electrolytes [6,10].

As OER activity is required for a rechargeable ZAB, we also evaluated the OER polarization curve of Fe-NBrGO in N_2 -saturated electrolytes. Overpotential at 10 mA cm^{-2} (η_{10}) and Tafel slope are used as the main parameters of OER activity. We used commercial Ir/C as the benchmark. In Figure 5a,b, Fe-NBrGO shows η_{10} of 476 and 615 mV, in 1 M KOH and 0.1 M PBS, respectively. OER kinetics of Fe-NBrGO are then evaluated using the Tafel slope (Figure 5c,d). Fe-NBrGO shows a lower Tafel slope of 138 mV dec^{-1} alkaline than that in neutral electrolyte (178 mV dec^{-1}). This implies that the kinetics reaction is faster in alkaline than in neutral electrolytes. A similar trend is also noticeable from the benchmark Ir/C. It shows a two-times increase in the Tafel slope from 70 to 153 mV dec^{-1} when employed in the neutral condition, which may correspond to a low concentration of hydroxyl ions that are needed during the OER process [6]. Notably, the Tafel slopes of Ir/C in alkaline and neutral electrolytes also show a different feature, which may indicate a difference in the rate-limiting step and surface coverage of OER intermediates in those two conditions [70].

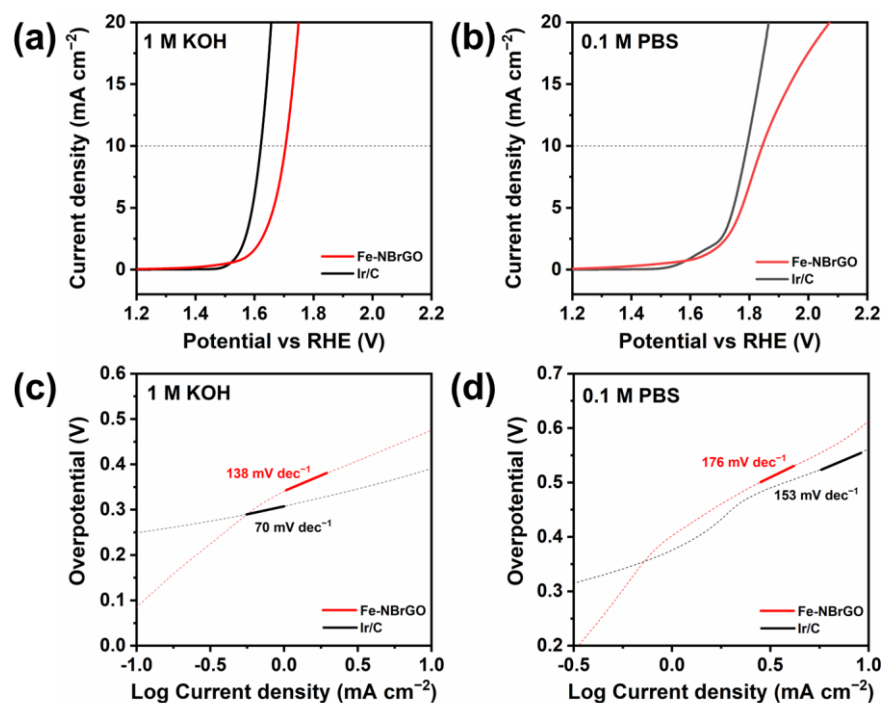


Figure 5. OER polarization curves of Fe-NBrGO and Ir/C in (a) 1 M KOH and (b) 0.1 M PBS. Tafel slope of Fe-NBrGO and Ir/C in (c) 1 M KOH and (d) 0.1 M PBS.

To validate the practical application of Fe-NBrGO, rechargeable ZABs with alkaline and neutral electrolyte were constructed using Fe-NBrGO as the air cathode (Figure 6a–c). First, discharge–charge polarization profiles were tested to assess the battery performance (Figure 6b). Fe-NBrGO shows smaller discharge–charge potential gaps in alkaline ZAB (6 M KOH + 0.15 M ZnO) than those in neutral ZAB (2 M KCl + 4 M NH_4Cl). This agrees with the higher ORR/OER activity of Fe-NBrGO in alkaline than in neutral electrolytes. In Figure 6c, alkaline ZAB with Fe-NBrGO exhibits a promising peak power density of 107 mW cm^{-2} , comparable to previous studies in the range of $62\text{--}123 \text{ mW cm}^{-2}$ [59,60,65,71]. For neutral ZAB, Fe-NBrGO can deliver a peak power density of 34 mW cm^{-2} , which is slightly higher than that of commercial Pt/C+Ir/C catalysts (29 mW cm^{-2} , Figure S7).

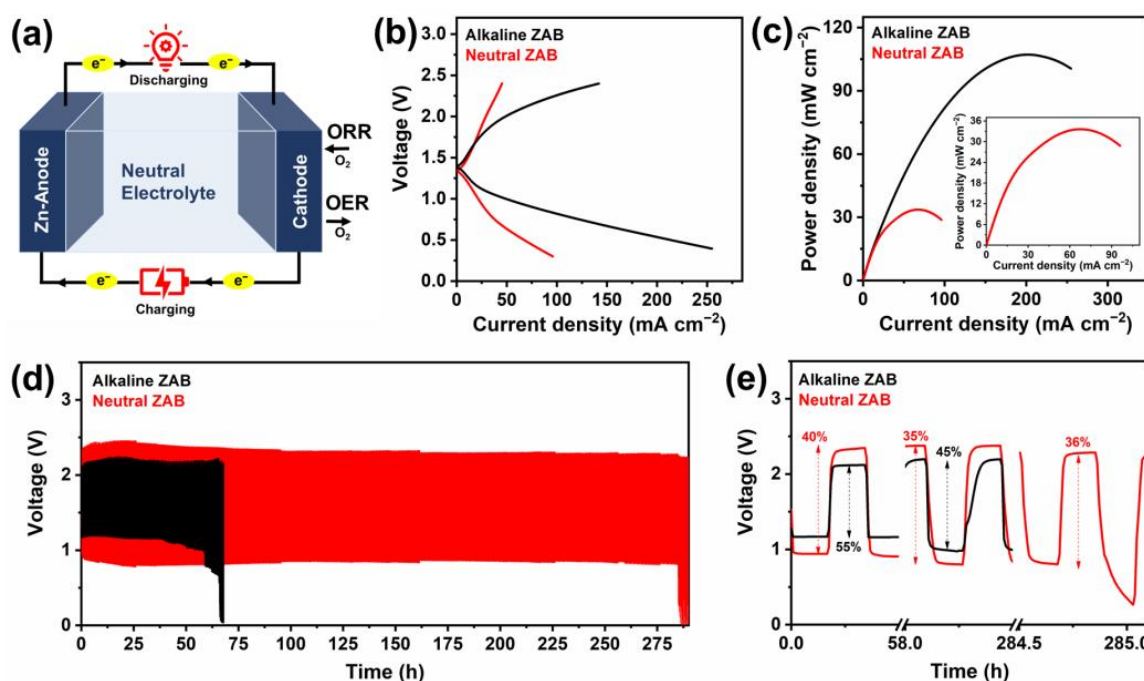


Figure 6. (a) Schematic illustration of ZAB. (b) Charging–discharging curves and (c) power density curves of alkaline and neutral ZAB with Fe-NBrGO. (d) Stability test and (e) voltaic efficiency of alkaline and neutral ZAB with Fe-NBrGO.

The stability of rechargeable ZAB with Fe-NBrGo was then evaluated from a discharge–charge cycling test at a current density of 10 mA cm^{-2} (Figure 6d). Noticeably, there is a more than three times increase in the battery’s cycle life with the usage of neutral electrolyte, compared to the alkaline one. Neutral ZAB with Fe-NBrGO shows stability for $\sim 284 \text{ h}$ of the cycling test, which outperforms some reported neutral ZABs using M-N/C catalysts that had cyclability in the range of 70–208 h (Table S5) [22,72,73]. The voltaic efficiency accounted for by dividing the discharging by the charging potential also confirms the high round-trip stability of the neutral ZAB. From Figure 6e, neutral ZAB has an initial voltaic efficiency of 40%, lower than that of the alkaline ZAB (55%). However, after 58 h of the cycling test, the efficiency of alkaline ZAB decreases by 10% just before it subsequently experiences failure. In contrast, neutral ZAB shows a 5% decrease in performance and could maintain a steady voltaic efficiency ($\sim 35\%$) throughout the remaining cycling test. The low cyclability of ZAB with alkaline electrolyte can be attributed to carbon corrosion at the air cathode and carbonate formation, which can reduce the electrolyte conductivity and block the pores of the air cathode [4,5,7,8].

The notable ORR/OER activity and high stability of neutral ZAB with Fe-NBrGO may be related to the following advantages: (1) N/B co-dopants modify the electronic structure of the carbon matrix, producing both N- and B-moieties active sites. (2) The homogeneous distribution of Fe nanoparticles encapsulated with N-doped carbon layers may facilitate both ORR/OER in a wide pH range and outstanding discharge–charge performance of ZABs in neutral electrolyte. (3) The 3D porous structure of rGO provides more accessible active sites. (4) Employing neutral electrolytes may inhibit carbon corrosion and not absorb CO₂, averting the formation of insoluble carbonates that may clog the pores of the air cathode, resulting in the stable performance of ZABs in neutral electrolyte.

4. Conclusions

In conclusion, we successfully synthesized iron-decorated N/B co-doped reduced graphene aerogel (Fe-NBrGO) as ORR/OER electrocatalysts in alkaline and neutral electrolytes. Fe-NBrGO has a 3D porous structure with homogeneously distributed carbon-encapsulated Fe nanoparticles. Fe-NBrGO is endowed with the synergistic effect of Fe-

containing active sites and N, B co-doping active sites that modify the electronic structure. As a result, Fe-NBrGO aerogel exhibits good ORR/OER activity in both alkaline and neutral electrolytes. The neutral rechargeable zinc-air battery with Fe-NBrGO also exhibits a promising performance with a long charge/discharge cycle life (~852 cycles) and a peak power density of 34 mW cm^{-2} . This study presents an effective method by combining hydrothermal synthesis and pyrolysis processes for producing a 3D porous structure of graphene aerogel with N/B-moieties and Fe-decorated nanoparticles for a highly stable neutral ZAB.

Supplementary Materials: The following supporting information can be downloaded at: <https://www.mdpi.com/article/10.3390/batteries9070356/s1>, Figure S1: XRD patterns of NBrGO after pyrolysis; Figure S2: Shifting in the (002) carbon peak of Fe-NBrGO after pyrolysis, compared to Fe-NBrGO before pyrolysis and pyrolyzed NBrGO; Figure S3: Deconvolution of Raman spectra of (a) GO, (b) NBrGO, and (c) Fe-NBrGO; Figure S4: SEM images with (a) SE mode and (b) BSE mode of Fe-NBrGO. (c) EDX elemental mapping of C, Fe, and O in Fe-NBrGO. Figure S5: Full XPS spectra of Fe-NBrGO; Figure S6: Cyclic voltammograms and corresponding double-layer capacitances of (a,b) NBrGO and (c,d) Fe-NBrGO in N_2 -saturated 1.0 M KOH; Figure S7: (a) Charging–discharging curves and (b) power density curves of alkaline and neutral ZAB with Pt/C + Ir/C; Table S1: Elemental composition of N 1s and B 1s of Fe-NBrGO from XPS measurement; Table S2: Elemental composition of Fe 2p of Fe-NBrGO from XPS measurement; Table S3: ORR performance of Fe-NBrGO and previously reported M-N/B co-doped carbon catalysts; Table S4: OER performance of Fe-NBrGO and previously reported M-N/B co-doped carbon catalysts; Table S5: Comparison of maximum power density (P_{\max}) and rechargeability of Fe-NBrGO in zinc-air batteries with previously reported Pt-free catalysts. (References [17,22,35,38,42,55,59,60,65,66,68,71–77] are cited in the Supplementary Materials).

Author Contributions: Conceptualization, Y.I., R.Y., F.I. and A.S.; methodology, Y.I. and A.S.; validation, R.Y., F.I. and A.S.; formal analysis, Y.I., F.B., P.B.P. and A.S.; investigation, Y.I., F.B., P.B.P., F.D., R.Y., F.I. and A.S.; resources, A.S.; data curation, Y.I.; writing—original draft preparation, Y.I., F.B. and P.B.P.; writing—review and editing, Y.I., F.B., P.B.P., F.D., R.Y., F.I. and A.S.; visualization, Y.I., F.B. and F.D.; supervision, R.Y., F.I. and A.S.; project administration, Y.I. and A.S.; funding acquisition, A.S. All authors have read and agreed to the published version of the manuscript.

Funding: The authors acknowledge financial support from Research, Community Service, and Innovation Program (P2MI) Institut Teknologi Bandung, 2022.

Data Availability Statement: Not applicable.

Acknowledgments: Y.I. thanks the National Research and Innovation Agency of Republic of Indonesia's Saintek Program for the doctoral scholarship. Y.I. acknowledges Andri Hardiansyah from Research Center for Advanced Materials BRIN for valuable discussion.

Conflicts of Interest: The authors declare no conflict of interest.

References

- Yin, M.; Miao, H.; Hu, R.; Sun, Z.; Li, H. Manganese Dioxides for Oxygen Electrocatalysis in Energy Conversion and Storage Systems Over Full pH Range. *J. Power Sources* **2021**, *494*, 229779. [[CrossRef](#)]
- Qiu, Q.; Pan, Z.-Z.; Yao, P.; Yuan, J.; Xia, C.; Zhao, Y.; Li, Y. A 98.2% energy efficiency Li-O₂ battery using a LaNi_{0.5}Co_{0.5}O₃ perovskite cathode with extremely fast oxygen reduction and evolution kinetics. *Chem. Eng. J.* **2023**, *452*, 139608. [[CrossRef](#)]
- Leong, K.W.; Wang, Y.; Ni, M.; Pan, W.; Luo, S.; Leung, D.Y.C. Rechargeable Zn-air batteries: Recent trends and future perspectives. *Renew. Sust. Energ. Rev.* **2022**, *154*, 111771. [[CrossRef](#)]
- Sumboja, A.; Ge, X.; Zheng, G.; Goh, F.W.T.; Hor, T.S.A.; Zong, Y.; Liu, Z. Durable rechargeable zinc-air batteries with neutral electrolyte and manganese oxide catalyst. *J. Power Sources* **2016**, *332*, 330–336. [[CrossRef](#)]
- Goh, F.T.; Liu, Z.; Hor, T.A.; Zhang, J.; Ge, X.; Zong, Y.; Yu, A.; Khoo, W. A near-neutral chloride electrolyte for electrically rechargeable zinc-air batteries. *J. Electrochem. Soc.* **2014**, *161*, A2080. [[CrossRef](#)]
- Wang, C.; Li, J.; Zhou, Z.; Pan, Y.; Yu, Z.; Pei, Z.; Zhao, S.; Wei, L.; Chen, Y. Rechargeable Zinc-Air Batteries with Neutral Electrolytes: Recent Advances, Challenges, and Prospects. *EnergyChem* **2021**, *3*, 100055. [[CrossRef](#)]
- Clark, S.; Mainar, A.R.; Iruin, E.; Colmenares, L.C.; Blázquez, J.A.; Tolchard, J.R.; Latz, A.; Horstmann, B. Towards rechargeable zinc-air batteries with aqueous chloride electrolytes. *J. Mater. Chem. A* **2019**, *7*, 11387–11399. [[CrossRef](#)]

8. Prakoso, B.; Mahbub, M.A.A.; Yilmaz, M.; Khoiruddin; Wenten, I.G.; Handoko, A.D.; Sumboja, A. Recent Progress in Extending the Cycle-Life of Secondary Zn-Air Batteries. *ChemNanoMat* **2021**, *7*, 354–367. [CrossRef]
9. Zhang, Y.; Deng, Y.-P.; Wang, J.; Jiang, Y.; Cui, G.; Shui, L.; Yu, A.; Wang, X.; Chen, Z. Recent Progress on Flexible Zn-Air Batteries. *Energy Stor. Mater.* **2021**, *35*, 538–549. [CrossRef]
10. Wu, W.-F.; Yan, X.; Zhan, Y. Recent progress of electrolytes and electrocatalysts in neutral aqueous zinc-air batteries. *Chem. Eng. J.* **2023**, *451*, 138608. [CrossRef]
11. Ma, R.; Lin, G.; Zhou, Y.; Liu, Q.; Zhang, T.; Shan, G.; Yang, M.; Wang, J. A review of oxygen reduction mechanisms for metal-free carbon-based electrocatalysts. *Npj Comput. Mater.* **2019**, *5*, 78. [CrossRef]
12. Feng, X.; Bai, Y.; Liu, M.; Li, Y.; Yang, H.; Wang, X.; Wu, C. Untangling the respective effects of heteroatom-doped carbon materials in batteries, supercapacitors and the ORR to design high performance materials. *Energy Environ. Sci.* **2021**, *14*, 2036–2089. [CrossRef]
13. Zhao, R.; Li, Q.; Chen, Z.; Jose, V.; Jiang, X.; Fu, G.; Lee, J.-M.; Huang, S. B, N-doped ultrathin carbon nanosheet superstructure for high-performance oxygen reduction reaction in rechargeable zinc-air battery. *Carbon* **2020**, *164*, 398–406. [CrossRef]
14. Xue, Y.; Yu, D.; Dai, L.; Wang, R.; Li, D.; Roy, A.; Lu, F.; Chen, H.; Liu, Y.; Qu, J. Three-dimensional B,N-doped graphene foam as a metal-free catalyst for oxygen reduction reaction. *Phys. Chem. Chem. Phys.* **2013**, *15*, 12220–12226. [CrossRef] [PubMed]
15. Chen, W.; Xu, L.; Tian, Y.; Li, H.; Wang, K. Boron and nitrogen co-doped graphene aerogels: Facile preparation, tunable doping contents and bifunctional oxygen electrocatalysis. *Carbon* **2018**, *137*, 458–466. [CrossRef]
16. Pei, Y.; Song, H.; Liu, Y.; Cheng, Y.; Li, W.; Chen, Y.; Fan, Y.; Liu, B.; Lu, S. Boron–nitrogen-doped carbon dots on multi-walled carbon nanotubes for efficient electrocatalysis of oxygen reduction reactions. *J. Colloid Interface Sci.* **2021**, *600*, 865–871. [CrossRef]
17. Cheng, R.; Li, K.; Li, Z.; Jiang, M.; Wang, F.; Yang, Z.; Zhao, T.; Meng, P.; Fu, C. Rational design of boron-nitrogen coordinated active sites towards oxygen reduction reaction in aluminum-air batteries with robust integrated air cathode. *J. Power Sources* **2023**, *556*, 232476. [CrossRef]
18. Hu, X.; Chen, K.; Guo, K.; Xiang, L.; Wen, Z.; Ci, S. N/B Co-doped carbon as metal-free cathode catalyst for high-performance asymmetric neutral-alkaline microbial fuel cell. *Electrochim. Acta* **2021**, *389*, 138518. [CrossRef]
19. Irmawati, Y.; Balqis, F.; Destyorini, F.; Adios, C.G.; Yudianti, R.; Iskandar, F.; Sumboja, A. Cobalt Nanoparticles Encapsulated with N-Doped Bamboo-Like Carbon Nanofibers as Bifunctional Catalysts for Oxygen Reduction/Evolution Reactions in a Wide pH Range. *ACS Appl. Nano Mater.* **2023**, *6*, 2708–2718. [CrossRef]
20. Rojas-Carbonell, S.; Artyushkova, K.; Serov, A.; Santoro, C.; Matanovic, I.; Atanassov, P. Effect of pH on the Activity of Platinum Group Metal-Free Catalysts in Oxygen Reduction Reaction. *ACS Catal.* **2018**, *8*, 3041–3053. [CrossRef]
21. Zhong, W.; Wang, Z.; Han, S.; Deng, L.; Yu, J.; Lin, Y.; Long, X.; Gu, M.; Yang, S. Identifying the Active Sites of a Single Atom Catalyst with pH-Universal Oxygen Reduction Reaction Activity. *Cell Rep. Phys. Sci.* **2020**, *1*, 100115. [CrossRef]
22. Wei, X.; Song, S.; Wu, N.; Luo, X.; Zheng, L.; Jiao, L.; Wang, H.; Fang, Q.; Hu, L.; Gu, W.; et al. Synergistically enhanced single-atomic site Fe by Fe₃C@C for boosted oxygen reduction in neutral electrolyte. *Nano Energy* **2021**, *84*, 105840. [CrossRef]
23. Ye, C.-W.; Xu, L. Recent advances in the design of a high performance metal–nitrogen–carbon catalyst for the oxygen reduction reaction. *J. Mater. Chem. A* **2021**, *9*, 22218–22247. [CrossRef]
24. García-Bordejé, E.; Víctor-Román, S.; Sanahuja-Parejo, O.; Benito, A.M.; Maser, W.K. Control of the microstructure and surface chemistry of graphene aerogels via pH and time manipulation by a hydrothermal method. *Nanoscale* **2018**, *10*, 3526–3539. [CrossRef]
25. Wang, X.; Zhang, Z.; Gai, H.; Chen, Z.; Sun, Z.; Huang, M. An efficient pH-universal electrocatalyst for oxygen reduction: Defect-rich graphitized carbon shell wrapped cobalt within hierarchical porous N-doped carbon aerogel. *Mater. Today Energy* **2020**, *17*, 100452. [CrossRef]
26. Xue, Q.; Ding, Y.; Xue, Y.; Li, F.; Chen, P.; Chen, Y. 3D nitrogen-doped graphene aerogels as efficient electrocatalyst for the oxygen reduction reaction. *Carbon* **2018**, *139*, 137–144. [CrossRef]
27. Hardiansyah, A.; Randy, A.; Dewi, R.T.; Angelina, M.; Yudasari, N.; Rahayu, S.; Ulfah, I.M.; Maryani, F.; Cheng, Y.-W.; Liu, T.-Y. Magnetic Graphene-Based Nanosheets with Pluronic F127-Chitosan Biopolymers Encapsulated & α-Mangosteen Drugs for Breast Cancer Cells Therapy. *Polymers* **2022**, *14*, 3163. [CrossRef]
28. Zheng, C.; Niu, S.; Lv, W.; Zhou, G.; Li, J.; Fan, S.; Deng, Y.; Pan, Z.; Li, B.; Kang, F.; et al. Propelling polysulfides transformation for high-rate and long-life lithium–sulfur batteries. *Nano Energy* **2017**, *33*, 306–312. [CrossRef]
29. Rodríguez-Mata, V.; González-Domínguez, J.M.; Benito, A.M.; Maser, W.K.; García-Bordejé, E. Reduced Graphene Oxide Aerogels with Controlled Continuous Microchannels for Environmental Remediation. *ACS Appl. Nano Mater.* **2019**, *2*, 1210–1222. [CrossRef]
30. Zhu, J.; Xiong, Z.; Zheng, J.; Luo, Z.; Zhu, G.; Xiao, C.; Meng, Z.; Li, Y.; Luo, K. Nitrogen-doped graphite encapsulated Fe/Fe₃C nanoparticles and carbon black for enhanced performance towards oxygen reduction. *J. Mater. Sci. Technol.* **2019**, *35*, 2543–2551. [CrossRef]
31. Luo, Y.; Zhang, J.; Chen, Y.; Li, Z.; Chen, J.; Wang, G.; Wang, R. MOF-derived porous carbon supported iron-based catalysts with optimized active sites towards oxygen reduction reaction. *J. Electroanal. Chem.* **2019**, *847*, 113191. [CrossRef]
32. Tylus, U.; Jia, Q.; Strickland, K.; Ramaswamy, N.; Serov, A.; Atanassov, P.; Mukerjee, S. Elucidating Oxygen Reduction Active Sites in Pyrolyzed Metal–Nitrogen Coordinated Non-Precious-Metal Electrocatalyst Systems. *J. Phys. Chem. C* **2014**, *118*, 8999–9008. [CrossRef]

33. Liang, Z.; Xia, W.; Qu, C.; Qiu, B.; Tabassum, H.; Gao, S.; Zou, R. Edge-Abundant Porous Fe_3O_4 Nanoparticles Docking in Nitrogen-Rich Graphene Aerogel as Efficient and Durable Electrocatalyst for Oxygen Reduction. *ChemElectroChem* **2017**, *4*, 2442–2447. [CrossRef]
34. Nugroho, A.; Wahyudhi, A.; Oktaviano, H.S.; Yudianti, R.; Hardiansyah, A.; Destyorini, F.; Irmawati, Y. Effect of Iron Loading on Controlling Fe/N-C Electrocatalyst Structure for Oxygen Reduction Reaction. *ChemistrySelect* **2022**, *7*, e202202042. [CrossRef]
35. Cao, L.; Wang, Y.; Zhu, Q.; Fan, L.; Wu, Y.; Li, Z.; Xiong, S.; Gu, F. Co/Co-N/Co-O Rooted on rGO Hybrid BCN Nanotube Arrays as Efficient Oxygen Electrocatalyst for Zn-Air Batteries. *ACS Appl. Mater. Interfaces* **2022**, *14*, 17249–17258. [CrossRef]
36. Ferrari, A.C.; Robertson, J. Interpretation of Raman spectra of disordered and amorphous carbon. *Phys. Rev. B* **2000**, *61*, 14095–14107. [CrossRef]
37. Hu, C.; Sedghi, S.; Silvestre-Albero, A.; Andersson, G.G.; Sharma, A.; Pendleton, P.; Rodríguez-Reinoso, F.; Kaneko, K.; Biggs, M.J. Raman Spectroscopy Study of The Transformation of The Carbonaceous Skeleton of A Polymer-Based Nanoporous Carbon Along The Thermal Annealing Pathway. *Carbon* **2015**, *85*, 147–158. [CrossRef]
38. Kang, X.; Fu, G.; Si, F.; Deng, X.; Wang, L.; Fu, X.-Z.; Luo, J.-L. Iron and boron-doped carbonized zeolitic imidazolate frameworks as efficient oxygen reduction electrocatalysts for Al-Air batteries. *Int. J. Hydrogen Energy* **2021**, *46*, 36221–36231. [CrossRef]
39. Wei, X.; Luo, X.; Wang, H.; Gu, W.; Cai, W.; Lin, Y.; Zhu, C. Highly-defective Fe-N-C catalysts towards pH-Universal oxygen reduction reaction. *Appl. Catal. B* **2020**, *263*, 118347. [CrossRef]
40. Wu, X.; Chen, K.; Lin, Z.; Zhang, Y.; Meng, H. Nitrogen doped graphitic carbon from biomass as non noble metal catalyst for oxygen reduction reaction. *Mater. Today Energy* **2019**, *13*, 100–108. [CrossRef]
41. Tian, H.; Liang, J.; Liu, J. Nanoengineering Carbon Spheres as Nanoreactors for Sustainable Energy Applications. *Adv. Mater.* **2019**, *31*, 1903886. [CrossRef] [PubMed]
42. Mahbub, M.A.A.; Adios, C.G.; Xu, M.; Prakoso, B.; LeBeau, J.M.; Sumboja, A. Red Bean Pod Derived Heterostructure Carbon Decorated with Hollow Mixed Transition Metals as a Bifunctional Catalyst in Zn-Air Batteries. *Chem. Asian J.* **2021**, *16*, 2559–2567. [CrossRef] [PubMed]
43. Li, D.; Han, Z.; Leng, K.; Ma, S.; Wang, Y.; Bai, J. Biomass wood-derived efficient Fe-N-C catalysts for oxygen reduction reaction. *J. Mater. Sci.* **2021**, *56*, 12764–12774. [CrossRef]
44. Sgarbi, R.; Kumar, K.; Jaouen, F.; Zitolo, A.; Ticianelli, E.A.; Maillard, F. Oxygen reduction reaction mechanism and kinetics on M-NxCy and M@N-C active sites present in model M-N-C catalysts under alkaline and acidic conditions. *J. Solid State Electrochem.* **2021**, *25*, 45–56. [CrossRef]
45. Noh, S.H.; Seo, M.H.; Kang, J.; Okajima, T.; Han, B.; Ohsaka, T. Towards a comprehensive understanding of FeCo coated with N-doped carbon as a stable bi-functional catalyst in acidic media. *NPG Asia Mater.* **2016**, *8*, e312. [CrossRef]
46. Li, Y.; Huang, J.; Hu, X.; Bi, L.; Cai, P.; Jia, J.; Chai, G.; Wei, S.; Dai, L.; Wen, Z. Fe Vacancies Induced Surface FeO_6 in Nanoarchitectures of N-Doped Graphene Protected β -FeOOH: Effective Active Sites for pH-Universal Electrocatalytic Oxygen Reduction. *Adv. Funct. Mater.* **2018**, *28*, 1803330. [CrossRef]
47. Mo, Q.; Chen, N.; Deng, M.; Yang, L.; Gao, Q. Metallic Cobalt@Nitrogen-Doped Carbon Nanocomposites: Carbon-Shell Regulation toward Efficient Bi-Functional Electrocatalysis. *ACS Appl. Mater. Interfaces* **2017**, *9*, 37721–37730. [CrossRef]
48. Wu, W.; Lin, F.; Yang, X.; Wang, B.; Lu, X.; Chen, Q.; Ye, F.; Zhao, S. Facile synthesis of magnetic carbon nanotubes derived from ZIF-67 and application to magnetic solid-phase extraction of profens from human serum. *Talanta* **2020**, *207*, 120284. [CrossRef]
49. Chen, T.; Cao, J.; Bao, X.; Peng, Y.; Liu, L.; Fu, W. Co nanoparticles decorated with N-doped carbon nanotubes as high-efficiency catalysts with intrinsic oxidase-like property for colorimetric sensing. *RSC Adv.* **2021**, *11*, 39966–39977. [CrossRef]
50. Wang, L.; Liang, K.; Deng, L.; Liu, Y.-N. Protein hydrogel networks: A unique approach to heteroatom self-doped hierarchically porous carbon structures as an efficient ORR electrocatalyst in both basic and acidic conditions. *Appl. Catal. B* **2019**, *246*, 89–99. [CrossRef]
51. Lin, L.; Zhu, Q.; Xu, A.-W. Noble-Metal-Free Fe-N/C Catalyst for Highly Efficient Oxygen Reduction Reaction under Both Alkaline and Acidic Conditions. *J. Am. Chem. Soc.* **2014**, *136*, 11027–11033. [CrossRef]
52. Jafari, M.; Gharibi, H.; Parnian, M.J.; Nasrollahpour, M.; Vafaee, M. Iron-Nanoparticle-Loaded Nitrogen-Doped Carbon Nanotube/Carbon Sheet Composites Derived from MOF as Electrocatalysts for an Oxygen Reduction Reaction. *ACS Appl. Nano Mater.* **2021**, *4*, 459–477. [CrossRef]
53. Li, C.; He, C.; Sun, F.; Wang, M.; Wang, J.; Lin, Y. Incorporation of Fe_3C and Pyridinic N Active Sites with a Moderate N/C Ratio in Fe-N Mesoporous Carbon Materials for Enhanced Oxygen Reduction Reaction Activity. *ACS Appl. Nano Mater.* **2018**, *1*, 1801–1810. [CrossRef]
54. Chisaka, M.; Iijima, T.; Ishihara, Y.; Suzuki, Y.; Inada, R.; Sakurai, Y. Carbon catalyst codoped with boron and nitrogen for oxygen reduction reaction in acid media. *Electrochim. Acta* **2012**, *85*, 399–410. [CrossRef]
55. Yuan, K.; Sfaelou, S.; Qiu, M.; Lützenkirchen-Hecht, D.; Zhuang, X.; Chen, Y.; Yuan, C.; Feng, X.; Scherf, U. Synergetic Contribution of Boron and Fe-N_x Species in Porous Carbons toward Efficient Electrocatalysts for Oxygen Reduction Reaction. *ACS Energy Lett.* **2018**, *3*, 252–260. [CrossRef]
56. Cao, C.; Wei, L.; Wang, G.; Shen, J. Superiority of boron, nitrogen and iron ternary doped carbonized graphene oxide-based catalysts for oxygen reduction in microbial fuel cells. *Nanoscale* **2017**, *9*, 3537–3546. [CrossRef]
57. Shi, J.; Shao, H.; Yang, F.; Li, J.; Fan, L.; Cai, W. Dual-template induced multi-scale porous Fe@FeNC oxygen reduction catalyst for high-performance electrochemical devices. *Chem. Eng. J.* **2022**, *445*, 136628. [CrossRef]

58. Wang, T.; Sun, C.; Yan, Y.; Li, F. Understanding the active sites of Fe–N–C materials and their properties in the ORR catalysis system. *RSC Adv.* **2022**, *12*, 9543–9549. [[CrossRef](#)]
59. Guo, Y.; Yuan, P.; Zhang, J.; Hu, Y.; Amiinu, I.S.; Wang, X.; Zhou, J.; Xia, H.; Song, Z.; Xu, Q.; et al. Carbon Nanosheets Containing Discrete Co-Nx-By-C Active Sites for Efficient Oxygen Electrocatalysis and Rechargeable Zn–Air Batteries. *ACS Nano* **2018**, *12*, 1894–1901. [[CrossRef](#)]
60. Gao, L.; Zhu, M.; Zhang, Z.; Cui, G. Cobalt-boron-oxide supported on N, P dual-doped carbon nanosheets as the trifunctional electrocatalyst and its application in rechargeable Zn-air battery and overall water-electrolysis. *Electrochim. Acta* **2019**, *327*, 134980. [[CrossRef](#)]
61. Wei, C.; Sun, S.; Mandler, D.; Wang, X.; Qiao, S.Z.; Xu, Z.J. Approaches for measuring the surface areas of metal oxide electrocatalysts for determining their intrinsic electrocatalytic activity. *Chem. Soc. Rev.* **2019**, *48*, 2518–2534. [[CrossRef](#)]
62. Sumboja, A.; Prakoso, B.; Ma, Y.; Irwan, F.R.; Hutani, J.J.; Mulyadewi, A.; Mahbub, M.A.A.; Zong, Y.; Liu, Z. FeCo Nanoparticle-Loaded Nutshell-Derived Porous Carbon as Sustainable Catalyst in Al-Air Batteries. *Energy Mater. Adv.* **2021**, *2021*, 738621. [[CrossRef](#)]
63. Liu, Z.; Guo, F.; Han, L.; Xiao, J.; Zeng, X.; Zhang, C.; Dong, P.; Li, M.; Zhang, Y. Manganese Oxide/Iron Carbide Encapsulated in Nitrogen and Boron Codoped Carbon Nanowire Networks as Accelerated Alkaline Hydrogen Evolution and Oxygen Reduction Bifunctional Electrocatalysts. *ACS Appl. Mater. Interfaces* **2022**, *14*, 13280–13294. [[CrossRef](#)] [[PubMed](#)]
64. Barua, A.; Paul, A. Synergistic Effect of Oxygen and Nitrogen Co-doping in Metal–Organic Framework-Derived Ultramicroporous Carbon for an Exceptionally Stable Solid-State Supercapacitor via a “Proton Trap” Mechanism. *Energy Fuels* **2021**, *35*, 10262–10273. [[CrossRef](#)]
65. Wang, Y.; Chen, Y.; Wang, Z.; Li, P.; Zhao, J.; Zhao, H.; Li, D.; He, T.; Wei, Y.; Su, Y.; et al. Boron doping induced electronic reconfiguration of Fe-N_x sites in N-doped carbon matrix for efficient oxygen reduction reaction in both alkaline and acidic media. *Int. J. Hydrogen Energy* **2022**, *47*, 18663–18674. [[CrossRef](#)]
66. Zhao, X.; Li, X.; Bi, Z.; Wang, Y.; Zhang, H.; Zhou, X.; Wang, Q.; Zhou, Y.; Wang, H.; Hu, G. Boron modulating electronic structure of FeN₄C to initiate high-efficiency oxygen reduction reaction and high-performance zinc-air battery. *J. Energy Chem.* **2022**, *66*, 514–524. [[CrossRef](#)]
67. Fajrial, A.K.; Saputro, A.G.; Agusta, M.K.; Rusydi, F.; Nugraha; Dipojono, H.K. First principles study of oxygen molecule interaction with the graphitic active sites of a boron-doped pyrolyzed Fe–N–C catalyst. *Phys. Chem. Chem. Phys.* **2017**, *19*, 23497–23504. [[CrossRef](#)]
68. Mulyadewi, A.; Mahbub, M.A.A.; Irmawati, Y.; Balqis, F.; Adios, C.G.; Sumboja, A. Rechargeable Zinc–Air Batteries with Seawater Electrolyte and Cranberry Bean Shell-Derived Carbon Electrocatalyst. *Energy Fuels* **2022**, *36*, 5475–5482. [[CrossRef](#)]
69. Wang, J.; Zhao, C.-X.; Liu, J.-N.; Ren, D.; Li, B.-Q.; Huang, J.-Q.; Zhang, Q. Quantitative kinetic analysis on oxygen reduction reaction: A perspective. *Nano Mater. Sci.* **2021**, *3*, 313–318. [[CrossRef](#)]
70. Antipin, D.; Risch, M. Calculation of the Tafel slope and reaction order of the oxygen evolution reaction between pH 12 and pH 14 for the adsorbate mechanism. *Electrochim. Sci. Adv.* **2022**, *e2100213*. [[CrossRef](#)]
71. Niu, H.-J.; Chen, S.-S.; Feng, J.-J.; Zhang, L.; Wang, A.-J. Assembled hollow spheres with CoFe alloyed nanocrystals encapsulated in N, P-doped carbon nanovesicles: An ultra-stable bifunctional oxygen catalyst for rechargeable Zn-air battery. *J. Power Sources* **2020**, *475*, 228594. [[CrossRef](#)]
72. Xu, R.; Wang, X.; Zhang, C.; Zhang, Y.; Jiang, H.; Wang, H.; Su, G.; Huang, M.; Toghan, A. Engineering solid–liquid–gas interfaces of single-atom cobalt catalyst for enhancing the robust stability of neutral Zn-air batteries under high current density. *Chem. Eng. J.* **2022**, *433*, 133685. [[CrossRef](#)]
73. Xu, Y.; Zhang, B.; Ran, J.; Liu, P.; Gao, D. Fe-based species anchored on N-doped carbon nanotubes as a bifunctional electrocatalyst for acidic/neutral/alkaline Zn–air batteries. *Nanotechnology* **2020**, *31*, 265402. [[CrossRef](#)]
74. Goh, F.W.T.; Liu, Z.; Ge, X.; Zong, Y.; Du, G.; Hor, T.S.A. Ag nanoparticle-modified MnO₂ nanorods catalyst for use as an air electrode in zinc–air battery. *Electrochim. Acta* **2013**, *114*, 598–604. [[CrossRef](#)]
75. Sabaa, H.M.; El-Khatib, K.M.; El-Kady, M.Y.; Mahmoud, S.A. Spinel structure of activated carbon supported MFe₂O₄ composites as an economic and efficient electrocatalyst for oxygen reduction reaction in neutral media. *J. Solid State Electrochem.* **2022**, *26*, 2749–2763. [[CrossRef](#)]
76. Tong, Y.; Chen, P.; Zhou, T.; Xu, K.; Chu, W.; Wu, C.; Xie, Y. A Bifunctional Hybrid Electrocatalyst for Oxygen Reduction and Evolution: Cobalt Oxide Nanoparticles Strongly Coupled to B,N-Decorated Graphene. *Angew. Chem. Int. Ed.* **2017**, *56*, 7121–7125. [[CrossRef](#)] [[PubMed](#)]
77. Gao, J.; Zhou, M.; Wang, X.; Wang, H.; Yin, Z.; Tan, X.; Li, Y. Preparing Co/N-Doped Carbon as Electrocatalyst toward Oxygen Reduction Reaction via the Ancient “Pharaoh’s Snakes” Reaction. *Batteries* **2022**, *8*, 150. [[CrossRef](#)]

Disclaimer/Publisher’s Note: The statements, opinions and data contained in all publications are solely those of the individual author(s) and contributor(s) and not of MDPI and/or the editor(s). MDPI and/or the editor(s) disclaim responsibility for any injury to people or property resulting from any ideas, methods, instructions or products referred to in the content.